Ouyang et al. *Zool. Res.* 2026, 47(1): 4−16
https://doi.org/10.24272/j.issn.2095-8137.2025.103
https://cstr.cn/32248.14.zr.2025.103

ZR | Zoological Research

Article Open Access

ARR3 variant-induced cone mosaicism alters cone subtype composition and disrupts phototransduction

Jiamin Ouyang[1,#], Zhen Yi[1,#], Yi Jiang[1,#], Xueqing Li[1,#], Gongpei Wang[1], Yingwei Wang[1], Wenting Du[1], Shuowei Chen[1], Yijun Dong[1], Xueshan Xiao[1], J. Fielding Hejtmancik[2], Wenmin Sun[1,*], Qingjiong Zhang[1,*]

[1] *State Key Laboratory of Ophthalmology*, *Zhongshan Ophthalmic Center*, *Sun Yat-sen University*, *Guangdong Provincial Key Laboratory of Ophthalmology and Visual Science*, *Guangzhou* 510623, *Guangdong Province*, *China*

[2] *Ophthalmic Genetics and Visual Function Branch*, *National Eye Institute*, *National Institutes of Health*, *Bethesda*, *MD* 20852, *USA*

ABSTRACT

Heterozygous variants in *ARR3*, encoding cone arrestin, have emerged as a frequent cause of early-onset high myopia with a unique X-linked female-limited inheritance pattern. However, the mechanistic basis for this unusual anti-X-linked pattern is still unclear. Developmental expression profiling in mice demonstrated robust Arr3 expression in the retina from postnatal day 14 onward, with localization confined predominantly to outer segments of cones marked by red/green opsins, including a subset co-labeled with both red/green and blue opsins. Retinal flatmounts from *Arr3* mutation knock-in mice and *Arr3* knockout rats revealed a mosaic pattern of Arr3 expression in heterozygous individuals. Retinal single-cell RNA sequencing revealed significant shifts in cone subtype proportions in *Arr3*$^{+/-}$ rats, with a marked reduction in M/S cones and a corresponding increase in S cones. Among differentially expressed genes, *Pde6h* was the only transcript altered in M/S cones across both *Arr3*$^{+/+}$ vs. *Arr3*$^{+/-}$ and *Arr3*$^{-/0}$ vs. *Arr3*$^{+/-}$ comparisons but not in *Arr3*$^{+/+}$ vs. *Arr3*$^{-/0}$. These findings suggest that heterozygous *Arr3* deficiency induces cone mosaicism that may mimic retinal defocus-like signals during phototransduction, potentially driving the development of high myopia under this distinctive inheritance model.

Keywords: *ARR3*; X-linked female-limited inheritance; Cones; Single-cell RNA sequencing

INTRODUCTION

The *ARR3* gene, located at Xq13.1, encodes arrestin 3 (also referred to as cone arrestin, X-arrestin, or arrestin 4), a phototransduction regulator expressed exclusively in retinal cones and the pineal gland (Murakami et al., 1993). As a member of the arrestin superfamily, arrestin 3 plays a critical role in terminating G protein-coupled receptor (GPCR) signaling by binding to phosphorylated, photoactivated cone opsins—such as red opsin encoded by *OPN1LW*—and dissociating them from heterotrimeric G proteins (e.g., transducin), thereby suppressing downstream effector activation (Gurevich & Gurevich, 2006; Murakami et al., 1993; Nikonov et al., 2008). In human beings, cone photoreceptors comprise three types (L, M, and S cones), which collectively mediate trichromatic color vision, visual acuity, and photopic sensitivity. However, rodents possess only M and S cones, which support dichromatic vision and vision under dim light (Brown & Wald, 1964; Carter-Dawson & Lavail, 1979). Arrestin 3 exhibits light-dependent intracellular translocation, accumulating in the cone outer segments under illumination and relocating to the inner segment in darkness (Zhang et al., 2003).

Our previous study identified the MYP26 (OMIM 301010) locus at Xq13.1 as responsible for a distinctive X-linked female-limited (XLFL) form of early-onset high myopia (eoHM), and first reported heterozygous *ARR3* variants as its causative factor (Xiao et al., 2016). Subsequent studies confirmed *ARR3*-associated MYP26 as the most prevalent Mendelian cause of eoHM with unique XLFL inheritance in Chinese and European cohorts (Haarman et al., 2022; Li et al., 2025; Liu et al., 2020; Széll et al., 2021; van Mazijk et al., 2022; Wang et al., 2023b; Yuan et al., 2021). Unlike conventional autosomal dominant, autosomal recessive, or X-linked recessive disorders, which typically arise through loss-of-function, gain-of-function, or dominant-negative mechanisms, the molecular basis for this novel XLFL transmission remains poorly understood. Investigations in affected individuals have been constrained by the lack of access to human retinal tissue, limiting functional insight into

Received: 16 June 2025; Accepted: 10 September 2025; Online: 11 September 2025

Foundation items: This work was supported by the National Natural Science Foundation of China (82471887), Science and Technology Planning Projects of Guangzhou (SL2024A03J00525), and Fundamental Research Funds of the State Key Laboratory of Ophthalmology

[#]Authors contributed equally to this work

*Corresponding authors, E-mail: sunwenmin@gzzoc.com; zhangqingjiong@gzzoc.com

the heterozygous variants in human beings with MYP26. In addition, prior studies in *Arr3* knockout mice have primarily focused on hemizygous and homozygous deletions, under the assumption that heterozygous variants in X-linked genes are phenotypically silent. Comparing to human hemizygous males with *ARR3* variants exhibiting no symptoms, *Arr3*-null mice demonstrate cone dystrophy, marked by significantly reduced cone density and diminished photopic responses (Deming et al., 2015). To date, although Arr3 is essential for maintaining cone photoreceptor function (Deming et al., 2015), no functional characterization of heterozygous *Arr3* variants has been reported in animal models. Given the importance of cone function in myopia development (Hagen et al., 2019; McClements et al., 2013; Taylor et al., 2018; Wang et al., 2013), the mechanism underlying the selective manifestation of eoHM that specific present in females with heterozygous *ARR3* variants rather than males with hemizygous *ARR3* variants remains unclear.

This study generated *Arr3* mutation knock-in mice and *Arr3* knockout rats to investigate the consequences of heterozygous *Arr3* disruption on retinal cone development and identity. To define the transcriptional landscape associated with this defect, single-cell RNA sequencing (scRNA-seq) was performed in *Arr3* knockout rat retinas, with emphasis on the heterozygous state implicated in XLFL-MYP26. The findings revealed cone subtype reorganization and cell-type-specific transcriptomic shifts, providing mechanistic insight into how heterozygous *ARR3* variants may drive female-limited eoHM.

MATERIALS AND METHODS

Generation of *Arr3* mutation knock-in mice and knockout rats

All animal experiments were approved by the Animal Use and Care Committee of Zhongshan Ophthalmic Center, Sun Yat-sen University (Approval No. 2019-153) and complied with the ARVO Statement for the Use of Animals in Ophthalmic and Vision Research. *Arr3* mutation knock-in mice and *Arr3* knockout rats were generated using CRISPR/Cas9-mediated genome editing as previously described (Cho et al., 2009). For the *Arr3* mutation knock-in mouse model, exon 13 of the murine *Arr3* gene was replaced with the c.928G>T/(p.E310*) variant, corresponding to the human *ARR3* c.928G>T/(p.E310*) variant identified in family F21 in our previous study (Wang et al., 2023b). The strategy to create *Arr3*$^{c.928G>T/+}$ (*Arr3*$^{M/+}$) heterozygous mice were generated as illustrated in Supplementary Figure S1. Two single-guide RNAs (sgRNAs) (Supplementary Table S1) were selected based on activity and specificity assays, and a P2A-EGFP cassette was inserted downstream of the stop codon in exon 17. For the *Arr3* knockout rat model, Cas9 mRNA and two sgRNAs (Supplementary Table S1), targeting intron 4 and intron 11 of *Arr3*, were co-injected into zygotes of Sprague Dawley rats, followed by transplantation into pseudopregnant females. Genotyping was performed by polymerase chain reaction (PCR) using genomic DNA extracted from tail tissue of newborn F0 pups. Primers used for genotyping are listed in Supplementary Table S1. Rodents were bred and housed under a 12 h light:12 h dark cycle at a controlled temperature (18–29°C) and humidity (40%–70%), with sufficient food and water provided. The gender of all animals is provided in Supplementary Table S2. Animals used for histological analyses were sacrificed under a daylight lamp between 2100h–2300h. A full list of experiments conducted in both models is presented in Supplementary Table S3.

Real-time Reverse Transcription PCR (RT-qPCR)

Total RNA was isolated from wild-type mouse retinas at embryonic day 13.5 (E13.5), E15.5, E17.5, postnatal day 1 (P1), P14, P21, and at 1, 2, 3, and 6 months of age (1M, 2M, 3M, and 6M). Reverse transcription was performed using a PrimerScript™ RT Reagent Kit (Takara, Japan). qPCR was conducted using PowerUp SYBR Green Master Mix and primers listed in Supplementary Table S1. Relative gene expression levels were calculated using the $2^{-\Delta\Delta Ct}$ method, with *Gapdh* used as the internal control. Each experiment was repeated in triplicate.

Western blotting and ProteinSimple Wes analysis

Retinal protein was extracted from mice and rats following transcardial perfusion with ice-cold saline. Tissue was lysed in RIPA buffer supplemented with protease inhibitors. Total protein concentration was determined using a Pierce™ BCA Protein Assay Kit (Thermo Fisher Scientific, USA). Equal amounts of lysate were separated via 7.5% sodium dodecyl sulphate-polyacrylamide gel electrophoresis (SDS-PAGE) and transferred to polyvinylidene fluoride (PVDF) membranes. The membranes were blocked in 5% skim milk for 1 h and incubated overnight at 4°C with rabbit anti-arrestin 3 (anti-Arr3). After washing, the membranes were incubated with horseradish peroxidase (HRP)-conjugated goat anti-rabbit IgG H&L for 1 h at room temperature (RT). Chemiluminescent signals were detected using a SuperSignal™ West Pico PLUS Kit (Thermo Fisher Scientific, USA) and imaged with the ChemiDoc Imaging System (Bio-Rad, USA). Membranes were then stripped using antibody stripping buffer, blocked in 5% skim milk for 1 h, and incubated at 4°C overnight with rabbit anti-β tubulin, followed by secondary antibody incubation and signal detection as described above. Due to low immunoreactivity of red/green and blue opsins in mouse and rat retinas by conventional western blotting, their expression was analyzed using the ProteinSimple Wes Simple Western system with a 12–230 kDa Master Kit (SM-W004, ProteinSimple, USA) according to the manufacturer's recommendations. Signals were processed using Compass software (ProteinSimple, USA). Antibody dilutions are detailed in Supplementary Table S1.

Ocular biometric measurements

Refractive state was assessed in awake animals using streak retinoscopy at a working distance of 33 cm. Prior to measurement, pupils were dilated with tropicamide and animals were dark-adapted for 30 min between 0900h and 1100h. Anesthesia was induced via intraperitoneal injection of 1% pentobarbital sodium (50 mg/kg) in mice and 2% pentobarbital sodium (100 mg/kg) in rats. Tropicamide was applied for pupil dilation, and methylcellulose was used to maintain corneal hydration. Ocular parameters of *Arr3* mutation knock-in mice and knockout rat were performed using spectral-domain optical coherence tomography (SD-OCT; Bioptigen Envisu R4310 OCT, Leica, Germany). Biometric parameters included axial length (AL), total retinal thickness (RT), vitreous chamber depth (VCD), lens thickness (LT), anterior chamber depth (ACD), and central corneal thickness (CCT). AL was measured from the anterior surface of the central cornea to the retinal pigment epithelium (RPE) layer. Retinal images were captured using B scan mode, while

other parameters were assessed using volume intensity scans. All images were centered on the optic nerve and processed using InVivoVue™ Diver v.2.4 software (Bioptigen, Germany). Measurements were obtained with ImageJ software. Fundus images, including posterior, nasal, temporal, dorsal, and ventral views, were captured using the Phoenix Micron IV system (Phoenix Research Labs, USA) and compared across genotypes.

Full-field electroretinography (ERG)

ERG recordings were conducted as previously described (Yi et al., 2020). Following 12 h of dark adaptation, *Arr3*$^{M/+}$ and *Arr3*$^{M/0}$ mice, along with age- and sex-matched control mice, were anesthetized under dim red light. Pupils were dilated using tropicamide. Scotopic ERG responses were recorded using increasing flash intensities of 0.003, 0.01, 0.03, 0.1, 0.3, 1.0, and 3.0 cd·s/m^2. After 5 min of light adaptation to a 20 cd·s/m^2 green background, photopic ERG responses were measured under six stimulus intensities (0.3, 1.0, 3.0, 10, 30, and 100 cd·s/m^2). For each flash intensity, 3–10 responses were averaged. Stimulus intervals ranged from 2–10 s for low intensities and up to 1 min for intensities above 3.0 cd·s/m^2.

Histological and immunohistochemical staining

Mice were euthanized and perfused transcardially with ice-cold saline. Eyes were enucleated and fixed in 4% paraformaldehyde (PFA). Paraffin embedding was performed, and 4 μm-thick sections were prepared for histological and immunohistochemical analysis. Hematoxylin and eosin (H&E) staining was carried out using hematoxylin and 1% eosin Y solution following standard deparaffinization and rehydration protocols. For immunohistochemistry, paraffin sections were subjected to antigen retrieval at 98°C for 30 min after deparaffinization and rehydration. Sections were blocked with 5% normal goat serum at RT for 30 min and incubated at 4°C overnight with primary antibodies, including rabbit anti-Arr3, rabbit anti-Opsin red/green, rabbit anti-Opsin blue, rabbit anti-Recoverin, mouse anti-Rhodopsin (1D4), rabbit anti-Pax6, mouse anti β-III tubulin, rabbit anti-α-PKC, and mouse anti-glutamine synthetase (GS). The sections were subsequently incubated at RT for 1 h with secondary antibodies, including Alexa Fluor 488 conjugated donkey anti mouse IgG and Alexa Fluor 568 conjugated donkey anti rabbit IgG. For co-labeling of Arr3 with other cone subtype markers, multiple immunohistochemistry (mIHC) was performed using a commercial kit according to the manufacturer's instructions. Fluorescence images were acquired using a LSM 980 Zeiss confocal microscope (Zeiss, Germany). Antibody dilutions are listed in Supplementary Table S1.

Retinal flatmount staining

Mice and rats were euthanized and perfused transcardially with ice-cold saline, after which retinas were carefully dissected and fixed in 4% PFA at RT for 40 min. Fixed retinas were rinsed three times in PBST (5 min each) and incubated overnight at 4°C in blocking solution containing 5% normal goat serum (NGS) with 0.5% Triton X-100. Retinas were then incubated overnight at 4 °C with primary antibodies, including rabbit anti-Arr3, rabbit anti-Opsin red/green, and rabbit anti-Opsin blue, followed by incubation with secondary antibody Alexa Fluor 568 conjugated donkey anti rabbit IgG at RT for 1 h. Whole-mount images were acquired using the TissueFAXS imaging system (TissueGnostics, Austria). Given the dorsal-ventral opsin expression gradient in the mouse retina—where M opsin dominates dorsally and S opsin ventrally—most cones co-express M and S opsins with spatial variability (Applebury et al., 2000). To minimize sampling bias, cone counts were conducted within two circular regions: (1) a central region defined by an inner circle 50 μm from the optic disc, with a surrounding annular zone extending an additional 15 μm; and (2) a middle region defined by an inner circle 100 μm from the optic disc, also surrounded by a 15 μm annular band.

ScRNA-seq analysis of *Arr3* knockout rats

At P14, rat retinas were collected following transcardial perfusion with ice-cold saline and enzymatically dissociated using 200 units papain (Worthington, LS003126) at 37°C for 30 min. Cell suspensions were submitted to BerryGenomics Co. Ltd. for scRNA-seq. Briefly, single cells were captured for reverse transcription and barcoding using gel bead-in-emulsion (GEM), followed by library construction and paired-end 150 bp sequencing on the Illumina NovaSeq platform (Illumina, USA). Downstream analysis was performed using the Omicsmart single-cell RNA-seq platform. Cells were clustered based on enrichment of gene markers (Supplementary Table S4) (Macosko et al., 2015). Clusters with low-quality transcriptomes or co-expression of more than five distinct major retinal cell-type markers were defined as doublets and excluded. As *Arr3* is cone-specific, cones were furthered classified into M cones, M/S cones, and S cones based on *Opn1mw* and *Opn1sw* expression. Subtype proportions and transcriptional profiles were compared among *Arr3*$^{+/-}$, *Arr3*$^{-/0}$, and wild-type rats. Differentially expressed genes (DEGs) were identified within each cone subtype and genotype group using thresholds of |fold change|>1 and P<0.05. Volcano plots and Venn diagrams were generated using the Omicsmart platform and OmicShare tools.

Statistical analysis

For pairwise comparisons of ocular biometric parameters, including AL, RT, VCD, LT, ACD, CCT, and refraction, two-tailed Student's *t*-tests were applied. For comparisons involving more than two groups, such as quantification of Arr3-positive cells, red/green and blue opsin-positive cells, and DEG expression, one-way analysis of variance (ANOVA) followed by Bonferroni correction was used. Proportional differences in cone subtypes across clusters (% of cones) was assessed using chi-squared tests. Statistical significance was defined as P<0.05 or 0.05/n for multiple comparisons, where n is the product of the number of groups and parameters tested. All analyses were conducted using IBM SPSS Statistics v.25.0. Histograms and line charts were generated using GraphPad Prism v.9.0, with error bars representing standard error of the mean (SEM).

RESULTS

Temporal and spatial expression pattern of Arr3 during retinal development

A temporal expression analysis in mouse retinas revealed no detectable *Arr3* mRNA during embryogenesis, followed by postnatal onset and progressive up-regulation during the course of refractive eye development (Figure 1A). By P14, coinciding with eye opening, *Arr3* mRNA expression reached relatively high levels (Figure 1A), suggesting a potential role for *Arr3* in postnatal emmetropization.

Immunostaining of mouse retinal sections was performed to

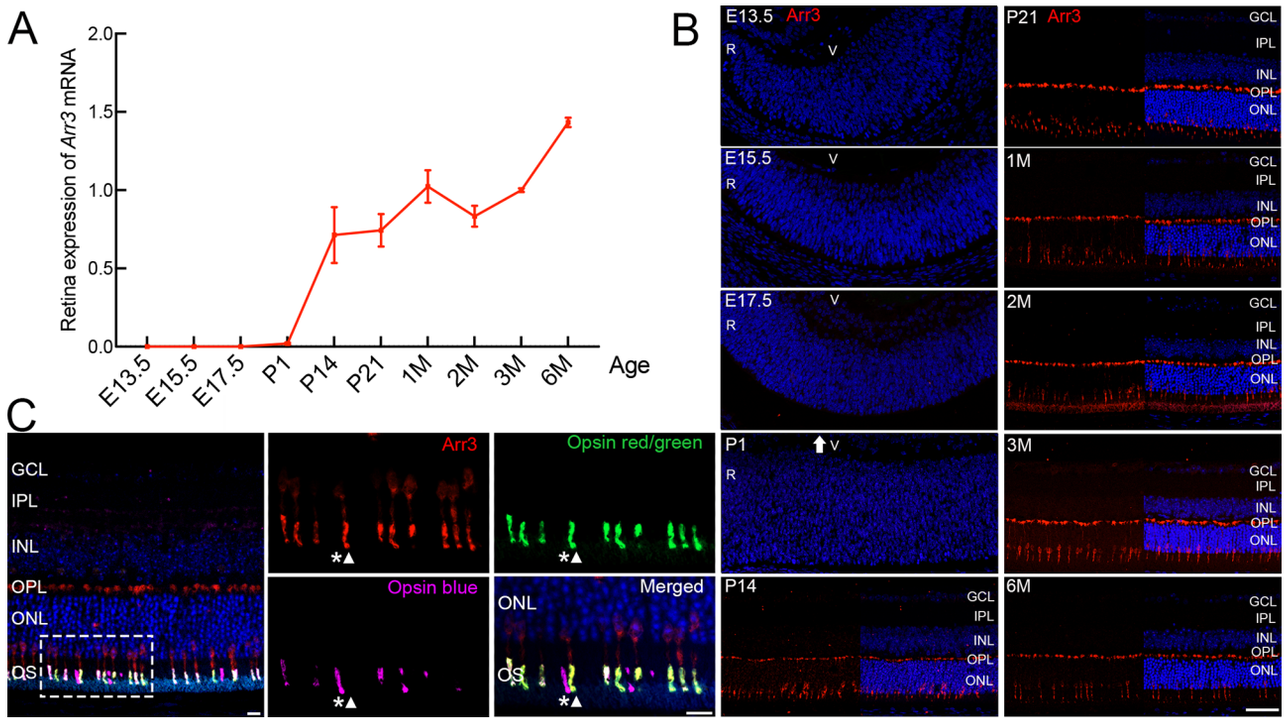

Figure 1 Expression profile of *Arr3* in the mouse retina

A: RT-qPCR analysis revealed a marked up-regulation of *Arr3* expression from P1 to P14 in wild-type mouse retina. E, embryonic day, P, post-natal day, M, month. B: Immunohistochemical analysis of retinas at corresponding developmental stages showed no detectable Arr3 signal at embryonic stages and P1. Expression was evident from P14, including P21, 1M, 2M, 3M, and 6M. Arr3 was localized primarily to photoreceptors and was highest in the outer plexiform layer, followed by photoreceptor layer. White arrow in P1 indicates direction toward the vitreous. V, vitreous. R, retina. GCL, retinal ganglion cell layer; IPL, inner plexiform layer; INL, inner nuclear layer; OPL, outer plexiform layer; ONL, outer nuclear layer. Scale bar: 50 μm. C: Arr3 was detected in outer segments of red/green opsin-positive cones, with a subset of these cells showing partial co-stained with both red/green opsin and blue opsin (triangle). Multiple immunohistochemical analysis of wild-type retina at 1M showed Arr3 was absent in true S cones labeled only with blue opsin (asterisk). Scale bar: 10 μm.

characterize Arr3 protein distribution over time. Consistent with transcript dynamics, Arr3 protein was absent at the embryonic stage (Figure 1B) and first detected at P14 (Figure 1B), in parallel with rising mRNA levels (Figure 1A). From P14 through to 6M, Arr3-positive cells were predominantly localized to the outer plexiform layer (OPL) and photoreceptor layer (Figure 1B). Similar spatial expression was observed in rat retinas (Supplementary Figure S2). High-magnification imaging of the photoreceptor layer revealed that Arr3 expression was specifically co-labeled with red/green opsin in outer segments of cones including some partially co-stained with both red/green opsin and blue opsin (Figure 1C). The observed expression profile aligns with the established role of Arr3 in opsin deactivation during phototransduction.

Arr3 deficiency in heterozygous rodents results in mosaic Arr3 expression

To investigate the functional consequences of *Arr3* disruption, *Arr3* mutation knock-in mice and knockout rats were generated using CRISPR-Cas 9 (Supplementary Figure S1A, C). The knock-in allele reproduced the human c.928G>T/(p.E310*) variant previously reported in our study (Wang et al., 2023b). Genotypes were confirmed by PCR (Supplementary Figure S1B, D). Protein analyses showed reduced Arr3 expression in $Arr3^{M/+}$ mice and absence of expression in $Arr3^{M/0}$ mice compared with $Arr3^{+/+}$ mice, consistent with findings in *Arr3* knockout rats (Supplementary Figure S1B, D).

Because *ARR3* variants are responsible for eoHM, ophthalmic phenotypes were further evaluated in both species (Supplementary Table S3). Streak retinoscopy revealed a tendency of myopic shift in $Arr3^{M/+}$ mice and $Arr3^{+/-}$ rats relative to wild-type controls (Supplementary Table S5). Ocular biometry demonstrated a mild increase in total retinal thickness in $Arr3^{M/+}$ mice and $Arr3^{+/-}$ rats at 1M (Supplementary Figure S3A–D and Table S6), whereas other ocular parameters, including AL, VCD, LT, ACD, and CCT, did not differ from wild-type animals (Supplementary Figure S4A, B and Table S6). No evidence of retinal degeneration was observed on fundus photography or H&E staining in $Arr3^{M/+}$ mice and $Arr3^{+/-}$ rats (Supplementary Figure S3E; Supplementary Figure S4C), and additional retinal markers showed no obvious differences (Supplementary Figure S5).

ERG analysis demonstrated reduced scotopic and photopic responses in $Arr3^{M/+}$ mice relative to sex-matched wild-type controls between 1M and 3M (Supplementary Figure S6A, B). In $Arr3^{M/+}$ mice, ERG waveforms remained variably preserved up to 5M, whereas signals in $Arr3^{+/+}$ mice declined after 3M (Supplementary Figure S6), resulting in relatively higher amplitudes in $Arr3^{M/+}$ mice at 5M. Photopic ERG amplitudes were significantly increased in $Arr3^{M/+}$ mice at 5M under stimulus intensities of 3.0, 10.0, 30.0, and 100.0 cd·s/m^2, while scotopic responses were higher at 0.3, 1.0, and 3.0 cd·s/m^2 (Supplementary Figure S6C).

Given the cone-specific expression of Arr3, retinal flatmount staining was performed to assess expression in mutant rodents. Wild-type retinas displayed uniform Arr3 expression without regional clustering (Figure 2; Supplementary Figure

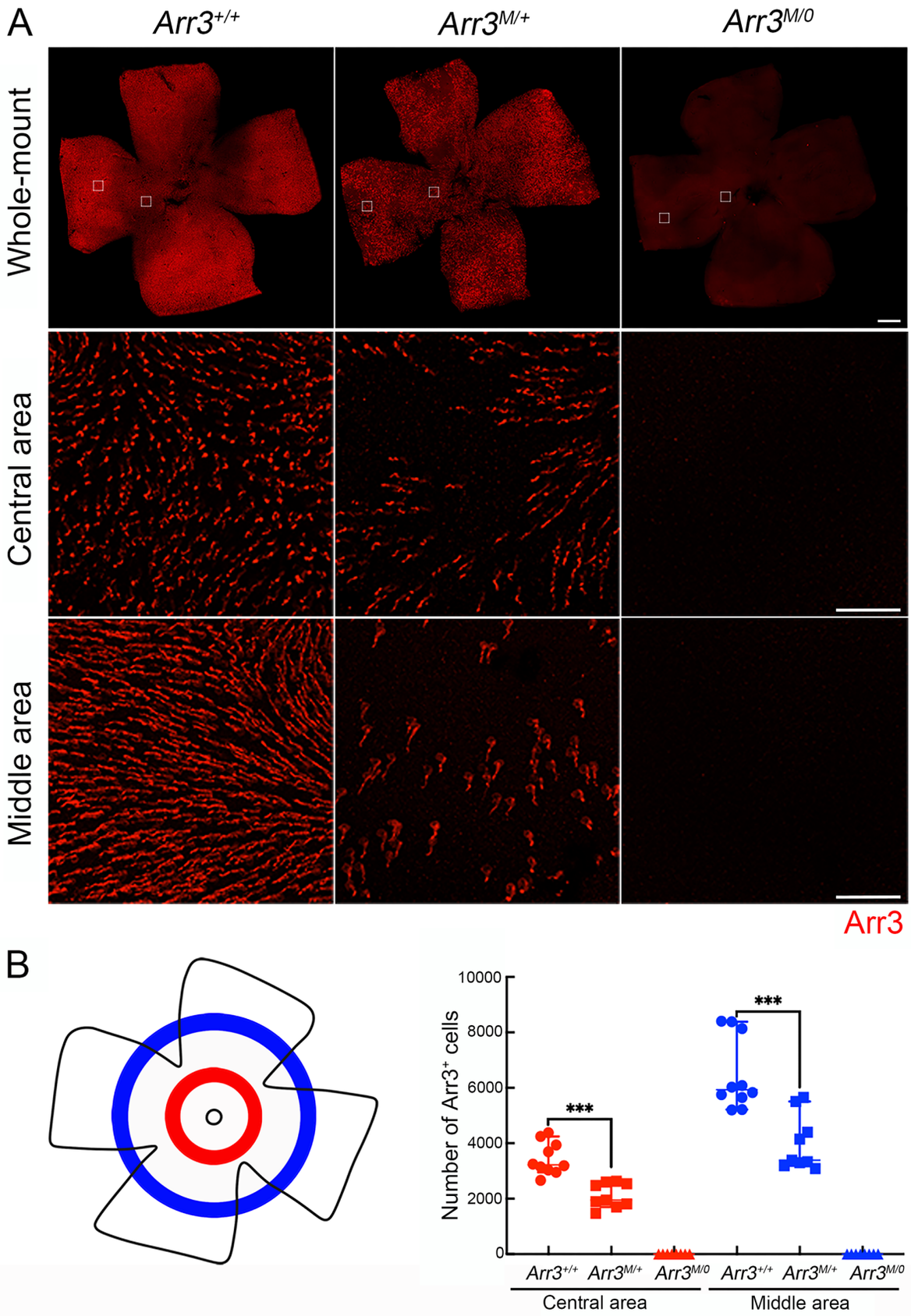

Figure 2 Retinal flatmounts of Arr3 expression in mice at 1M

A: Retinal flatmount images from *Arr3*$^{+/+}$, *Arr3*$^{M/+}$, and *Arr3*$^{M/0}$ mice at 1M, including whole-mount, central, and middle areas. A mosaic expression of Arr3 staining was identified in *Arr3*$^{M/+}$ mice compared to *Arr3*$^{+/+}$ mice. Scale bar: 500 μm in whole-mount; 50 μm in central and middle areas. B: Quantification of Arr3-positive cones in central and middle areas. Fewer Arr3-positive cones were observed in the central and middle areas in *Arr3*$^{M/+}$ mice compared to *Arr3*$^{+/+}$ mice (P=2.00×10^{-6} for central area, P=3.80×10^{-5} for middle area). ***: P<0.001.

S7). In contrast, compared with *Arr3*$^{+/+}$ mice, *Arr3*$^{M/+}$ mice exhibited a marked reduction and irregular distribution of Arr3-positive cones across the retina (Figure 2; Supplementary Figure S8), producing a mosaic pattern. No Arr3-positive cells were detected in *Arr3*$^{M/0}$ mice at 1M (Figure 2A). Comparable patterns were observed in *Arr3*$^{+/-}$ and *Arr3*$^{-/0}$ rats (Supplementary Figure S9). Quantitative analysis confirmed significant reductions in Arr3-positive cones in both central and middle retinal regions of *Arr3*$^{M/+}$ mice relative to wild-type controls at 1M (Figure 2B). These findings suggest that heterozygous *Arr3* loss eliminates Arr3 expression in a subset of cones, resulting in a characteristic mosaic pattern.

Altered cone subtype composition in *Arr3* heterozygous rodents

Given the mosaic expression of Arr3 observed in *Arr3* heterozygotes, scRNA-seq was performed on retinas from *Arr3*$^{+/+}$, *Arr3*$^{+/-}$, and *Arr3*$^{-/0}$ rats at P14 to investigate the molecular basis underlying the XLFL inheritance pattern. Droplet-based scRNA-seq yielded 32 950, 53 522, and 42 413 high-quality single-cell transcriptomes from wild-type, heterozygous, and hemizygous knockout retinas, respectively. A total of 26 transcriptional clusters were detected and categorized into nine major retinal cell types, including rod photoreceptors, cone photoreceptors, bipolar cells (BCs), retinal ganglion cells (RGCs), amacrine cells (ACs)/horizontal cells (HCs), astrocytes/Müller glia, microglia, endothelial cells (Endo), and retinal pigment epithelium (RPE), based on known cell-specific markers (Figure 3A, B). Clusters expressing more than three lineage-specific markers were excluded as potential doublets. All clusters were detected across samples and genotypes, and overall cell type composition was comparable among groups (Supplementary Figure S10A).

As Arr3 is essential for maintaining cone photoreceptor function, cone photoreceptors were further subclustered into three subtypes—M cones, S cones, and M/S cones—based on *Opn1mw* and *Opn1sw* (L cones are absent in rodents) (Figure 3C). Uniform Manifold Approximation and Projection (UMAP) confirmed distinct spatial segregation of the three subtypes across genotypes (Figure 3C). The distribution of M cones, M/S cones, and S cones differed among *Arr3*$^{+/+}$, *Arr3*$^{+/-}$, and *Arr3*$^{-/0}$ rats (Figure 3C). Although M cones accounted for similar proportions across all groups (*Arr3*$^{+/+}$: 66.05%, *Arr3*$^{+/-}$: 67.65%, *Arr3*$^{-/0}$: 67.50%), heterozygous retinas showed a significant reduction in M/S cones (11.74% vs. 27.84%) and a corresponding increase in S cones (20.60% vs. 6.10%) compared to wild-type (Figure 3D). A similar trend was observed in *Arr3*$^{-/0}$ retinas (M/S cones: 8.70%, S cones: 23.80%), although the difference in S cone proportion between *Arr3*$^{+/-}$ and *Arr3*$^{-/0}$ did not reach statistical significance (Figure 3D). Enrichment analysis using the ratio of observed to expected (RO/E) cell numbers further supported altered distribution of cone subtypes in mutant retinas, with M/S and S cones showing consistent shifts in *Arr3*$^{+/-}$ and *Arr3*$^{-/0}$ groups (Figure 3E).

To validate the transcriptomic findings, retinal flatmounts were immunostained with subtype-specific markers: opsin red/green (M cones) and opsin blue (S cones). Quantitative analysis showed no significant differences in the number or spatial distribution of marker-positive cones across genotypes (Supplementary Figures S11, S12). The lack of statistical significance for opsin blue-positive cells may reflect overlapping expression in both S and M/S cones, whose combined numbers were comparable across the three groups of mice. To further clarify cone morphology, co-labeling of opsin red/green, opsin blue, and Arr3 was performed in *Arr3*$^{M/+}$ mice. These mice exhibited structural disorganization of the cone outer segments, a phenotype absent in *Arr3*$^{+/+}$ and *Arr3*$^{M/0}$ mice (Figure 4). ProteinSimple Wes analysis showed a significant reduction in opsin red/green in *Arr3*$^{M/+}$ mice relative to wild-type controls (Supplementary Figure S13), a change not observed in *Arr3*$^{+/-}$ rats (Supplementary Figure S13). In addition, opsin blue expression showed an upward, albeit non-significant, trend in both *Arr3*$^{M/+}$ mice and *Arr3*$^{+/-}$ rats (Supplementary Figure S13).

Reduced *Pde6h* expression and disrupt phototransduction in *Arr3*$^{+/-}$ rats based on scRNA-seq

To investigate the molecular basis of cone subtype alterations, DEG analysis was performed using scRNA-seq data. Notably, results revealed 132 up-regulated and 253 down-regulated genes between *Arr3*$^{+/+}$ and *Arr3*$^{+/-}$ rats, nine up-regulated and 30 down-regulated genes between *Arr3*$^{-/0}$ and *Arr3*$^{+/-}$ rats, and 122 up-regulated and 226 down-regulated genes between *Arr3*$^{+/+}$ and *Arr3*$^{-/0}$ rats (Figure 5A).

Venn-network analysis was used to visualize shared and unique DEGs across the three pairwise comparisons: DEGs 1 (*Arr3*$^{+/+}$ vs. *Arr3*$^{+/-}$ rats), DEGs 2 (*Arr3*$^{-/0}$ vs. *Arr3*$^{+/-}$ rats), and DEGs 3 (*Arr3*$^{+/+}$ vs. *Arr3*$^{-/0}$ rats). To identify genes potentially involved in heterozygous dysfunction, overlap between DEGs 1 and DEGs 2 was prioritized. In M cones, six genes (*LOC108348108*, *Grk5*, *Ndufb1*, *Ndufa3*, *Hsph1*, and *Suv39h2*) were shared between DEGs 1 and DEGs 2 (Figure 5B). In M/S cones, four genes (*LOC108348108*, *Cplx4*, *Pde6h*, and *Hspa1b*) were shared between DEGs 1 and DEGs 2 (Figure 5C). In S cones, only *Tomm7* and *LOC103693330* overlapped in DEGs 1 and DEGs 2 (Figure 5D). Of these, *Pde6h*—a cone-specific gene involved in phototransduction—was uniquely expressed in cones.

Given that *Pde6h* encodes a cone-specific component of the phototransduction cascade (Gillespie & Beavo, 1988), the expression of additional phototransduction-related genes was examined across cone subtypes and genotypes. In M/S cones, *Pde6h* expression was down-regulated in *Arr3*$^{+/-}$ rats compared to both *Arr3*$^{+/+}$ and *Arr3*$^{-/0}$ rats, consistent with earlier (Figure 5E). *Gngt2* was down-regulated across all three genotypes. *Pde6c* expression was reduced in *Arr3*$^{+/-}$ rats relative to *Arr3*$^{-/0}$ rats but increased in *Arr3*$^{-/0}$ rats compared to *Arr3*$^{+/+}$ rats. In contrast, *Cngb3* and *Gnb3* were down-regulated only in *Arr3*$^{+/-}$ compared to *Arr3*$^{+/+}$ rats, with no significant changes observed in the remaining comparisons. In M cones, no DEGs were detected between *Arr3*$^{-/0}$ and *Arr3*$^{+/-}$ rats, while in S cones, *pde6h* was the only gene down-regulated. UMAP results further confirmed reduced *Pde6h* expression in *Arr3*$^{+/-}$ retinas compared to both *Arr3*$^{+/+}$ and *Arr3*$^{-/0}$ (Figure 5F). This reduction was restricted to M and M/S cones, with no change detected in S cones (Figures 5G, H; Supplementary Figure S10B–D). RT-qPCR analysis showed a consistent down-regulation trend for *Pde6h*, *Pde6c*, and *Gngt2* in both *Arr3*$^{M/+}$ mice and *Arr3*$^{+/-}$ rats compared to their wild-type counterparts, although the differences did not reach statistical significance (Supplementary Figure S14). ProteinSimple Wes analysis revealed a similar down-regulation trend for *Pde6h* in both models (Supplementary Figure S14).

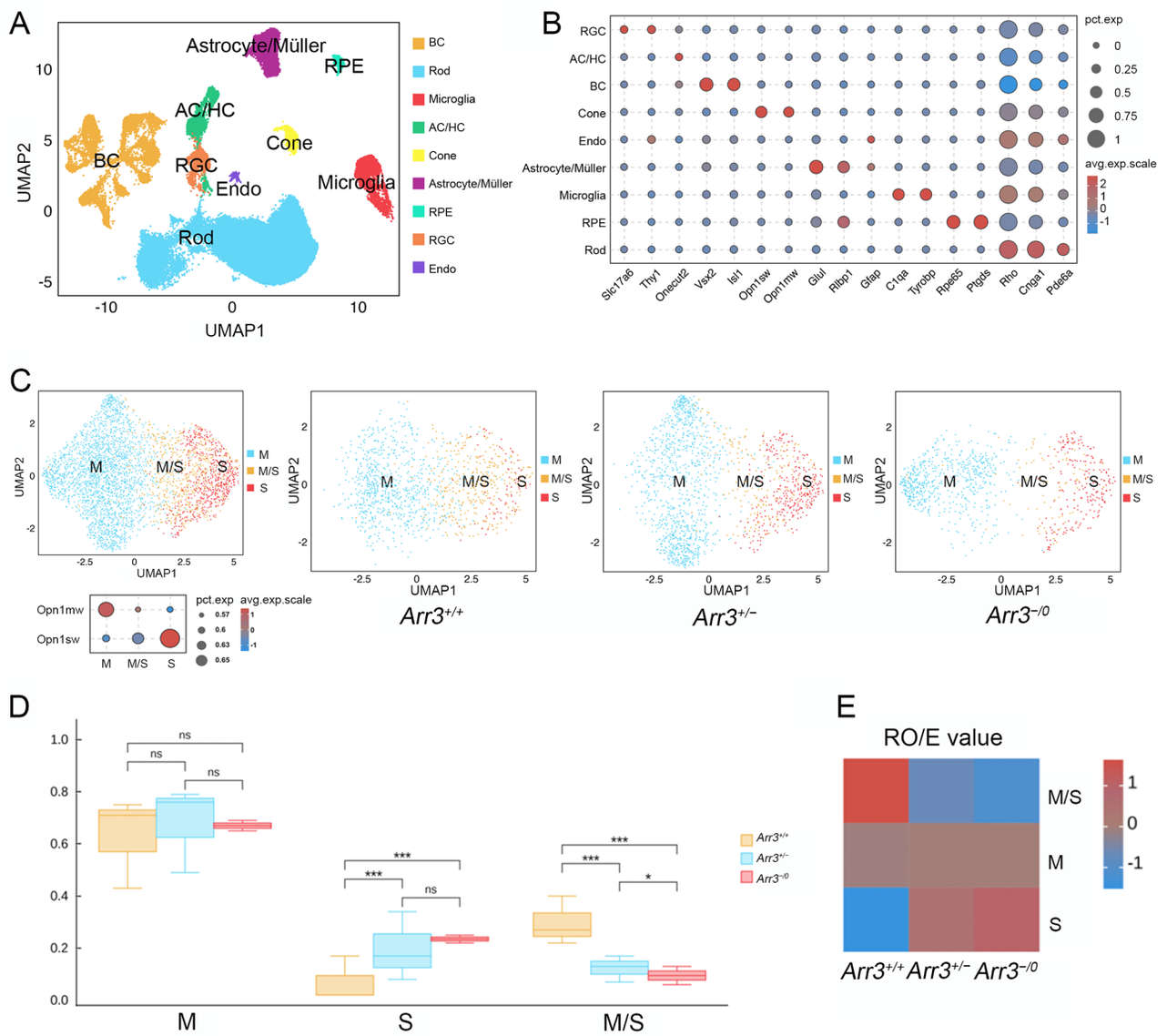

Figure 3 Single-cell transcriptomic analysis of cones from P14 retinas in *Arr3* knockout rats

A, B: Uniform Manifold Approximation and Projection (UMAP) plots of retinal cells from *Arr3*$^{+/+}$, *Arr3*$^{+/-}$, and *Arr3*$^{-/0}$ rats revealed nine retinal cell clusters, including retinal ganglion cells (RGCs), amacrine cells (ACs)/horizontal cells (HCs), bipolar cells (BCs), endothelial cell (Endo), cones, rods, retinal pigment epithelium (RPE), microglia, and astrocyte/Müller cells, based on canonical markers. C: Cones were further subdivided into three clusters based on *Opn1mw* and *Opn1sw* expression, including M cones, S cones, and M/S cones. UMAP visualization showed the distribution of cone subtypes across genotypes. D: Compared with *Arr3*$^{+/+}$ rats, *Arr3*$^{+/-}$ rats exhibited a significant reduction in M/S cones and an increase in S cones (P=5.74×10^{-26} for M/S cones, and P=1.55×10^{-26} for S cones). M/S cone proportions also differed significantly between *Arr3*$^{+/-}$ and *Arr3*$^{-/0}$ rats. ns: Not significant; *: P<0.05; ***: P<0.001. E: RO/E values indicated statistically significant differences in M/S and S cones in *Arr3*$^{+/-}$ and *Arr3*$^{-/0}$ rats. pct. exp, percent expressed. avg.exp.scale, average expression scaled.

DISCUSSION

This study established two rodent models—*Arr3* mutation knock-in mice and *Arr3* knockout rats—to explore the pathogenic basis of the unique XLFL inheritance pattern identified in eoHM caused by heterozygous variants of *ARR3* (MYP26). Spatiotemporal analysis demonstrated that Arr3 expression in rodents followed a developmental pattern similar to that of red/green opsin. Retinal flatmounts revealed a characteristic mosaic expression pattern in heterozygous *Arr3*$^{M/+}$ mice and *Arr3*$^{+/-}$ rats. Furthermore, scRNA-seq identified altered cone subtype proportions in *Arr3* heterozygous rats, including a marked reduction in M/S cones and a corresponding expansion of S cones. Notably, expression of *Pde6h*, a key effector in cone phototransduction, was diminished in M/S cones of *Arr3* heterozygous rats. These findings support a model in which heterozygous *Arr3* loss induces cone mosaicism that resulting disrupting cone subtype composition and phototransduction homeostasis, potentially generating conflicting visual signals that mimic optical defocus and trigger abnormal emmetropization.

Cone arrestin, encoded by *ARR3*, functions as one of two visual arrestins in mammals and mediates opsin desensitization in cone photoreceptors. The mosaic loss of ARR3 resulting from heterozygous variants may induce spatially heterogeneous cone responses and unbalanced visual signaling, disrupting downstream processing in retinal

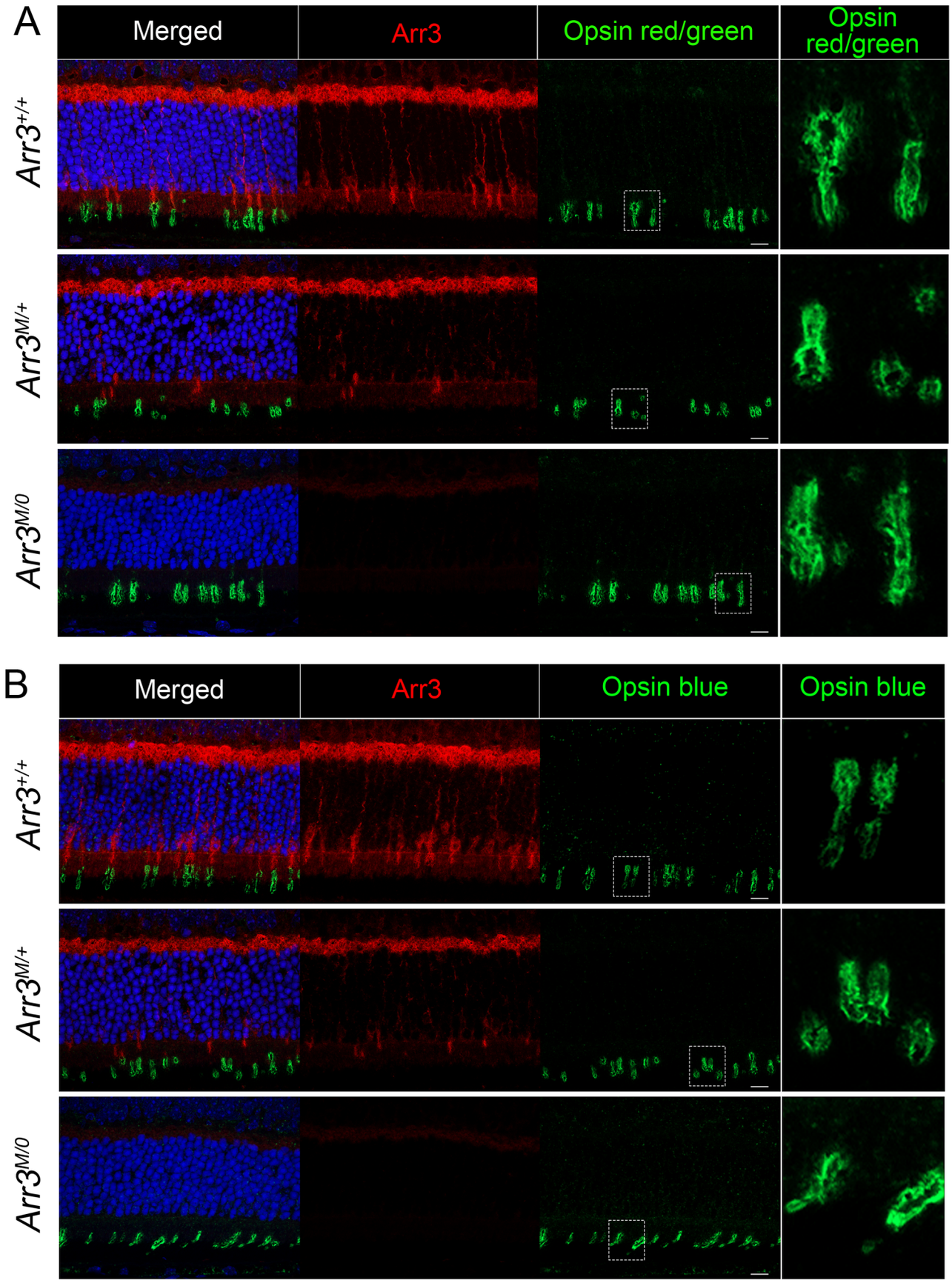

Figure 4 Co-labeling of red/green and blue opsin with Arr3 in *Arr3* mutation knock-in mice

A, B: Morphological disorganization was observed in the outer segments of *Arr3*$^{M/+}$ mice compared to *Arr3*$^{+/+}$ and *Arr3*$^{M/0}$ mice. Fewer Arr3-positive cells were detected in *Arr3*$^{M/+}$ mice relative to *Arr3*$^{+/+}$ mice, and no Arr3 expression was observed in *Arr3*$^{M/0}$ mice. Scale bar: 10 μm.

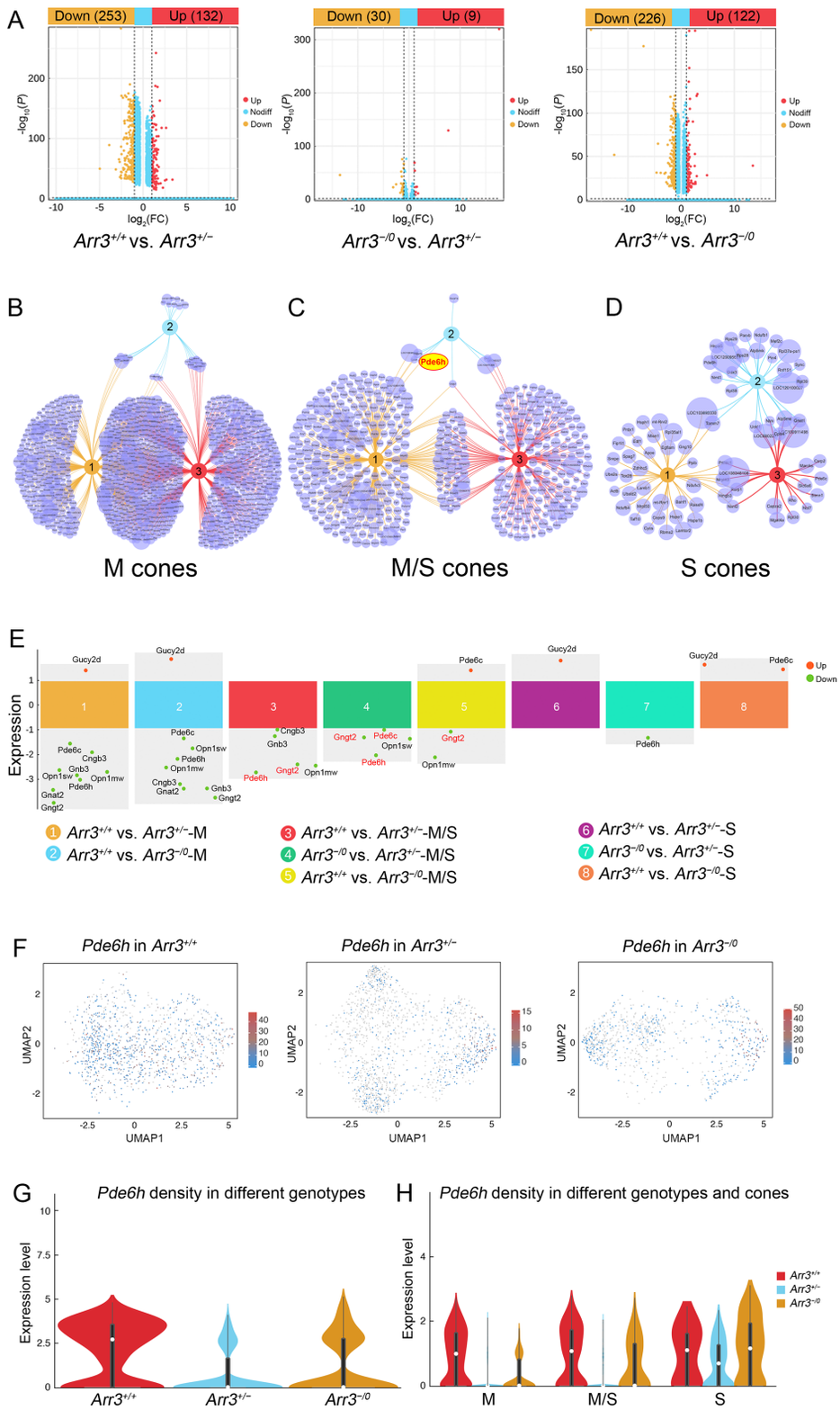

Figure 5 Analysis of scRNA-seq-derived differentially expressed genes (DEGs) from retinas of *Arr3* knockout rats at P14

A: Volcano plot showing DEGs in three pairwise comparisons: *Arr3*$^{+/+}$ vs. *Arr3*$^{+/-}$ rats (group 1), *Arr3*$^{-/0}$ vs. *Arr3*$^{+/-}$ rats (group 2), and *Arr3*$^{+/+}$ vs. *Arr3*$^{-/0}$ rats (group 3). In *Arr3*$^{+/+}$ vs. *Arr3*$^{+/-}$ rats, 132 genes were up-regulated and 253 genes were down-regulated in *Arr3*$^{+/-}$ rats. For *Arr3*$^{-/0}$ vs. *Arr3*$^{+/-}$ rats, nine genes were up-regulated and 30 genes were down-regulated in *Arr3*$^{+/-}$ rats. For *Arr3*$^{+/+}$ and *Arr3*$^{-/0}$ rats, 122 genes were up-regulated and 226 genes were down-regulated. Nodiff, no difference. B–D: Venn network diagrams showing DEGs shared or unique across three pairwise comparisons for each cone subtype (M cones, M/S cones, and S cones). In M/S cones, *Pde6h* was the only DEG shared between the *Arr3*$^{+/+}$ vs. *Arr3*$^{+/-}$ rats and *Arr3*$^{-/0}$ vs. *Arr3*$^{+/-}$ rats but was not shared in *Arr3*$^{+/+}$ vs. *Arr3*$^{-/0}$ rats. E: Differential expression scatter plot of phototransduction-related genes. Green circles indicate down-regulation and red circles indicate up-regulation. Genes in red indicate statistically significant differences. M, M cones; M/S, M/S cones; S, S cones. F: UMAP visualization of *Pde6h* expression across genotypes. G, H: Violin plots showing reduced *Pde6h* expression in M and M/S cones of *Arr3*$^{+/-}$ rats.

circuitry and initiating the pathological cascade leading to eoHM (Xiao et al., 2016; Wang et al., 2023a, 2023b). This mechanism parallels that proposed for *OPN1LW*-associated eoHM, in which haplotypes or truncation variants eliminate red photopigment expression in a subset of L cones, generating a retinal mosaic of functional and non-functional red cones (Li et al., 2015; McClements et al., 2013; Wang et al., 2023a). The resulting differential inputs to bipolar cells are thought to perturb signal integration and promote axial elongation (Wang et al., 2023a). In the present study, *Arr3*$^{M/+}$ mice and *Arr3*$^{+/-}$ rats exhibited mosaic reduction of Arr3 expression, suggesting selective loss across cone subtypes. ScRNA-seq further revealed a marked reduction of M/S cones and a corresponding increase in S cones in *Arr3* heterozygous mutants. These results confirmed that incomplete loss of Arr3 produced mosaic effects on different cone subtypes, leading to a compositional shift. This finding is consistent with prior observations in patients with eoHM carrying *ARR3* or *OPN1LW* variants.

ARR3-associated eoHM manifested in about 97% of heterozygous females but in only 33.3% of hemizygous males, showing a pattern of XLFL inheritance (Wang et al., 2023b). To date, diseases with XLFL has been only discovered in variants from two genes, *PCDH19* (Dibbens et al., 2008) and *ARR3* (Xiao et al., 2016). In *PCDH19*-associated XLFL cognitive impairment, recent mouse models have demonstrated heterozygous variants result in cellular mosaicism through random X-chromosome inactivation, leading to spatial mismatches between PCDH19 and N-cadherin-expressing neurons and impaired formation of hippocampal mossy fiber synapses (Giansante et al., 2024; Hoshina et al., 2021). However, the situation of *ARR3*-associated XLFL may be different, of which female patients with heterozygous variants in *ARR3* manifest eoHM with a mild impairment of cone functions. This divergence likely reflects the specialized microcircuitry of the cone system, wherein photoreceptors with distinct spectral sensitivities are organized into spatially integrated mosaics, and the role of ARR3 in terminating cone phototransduction through opsin binding and deactivation. Cones, mediating daylight vision, contain several types of visual pigments with different absorption spectra, enabling visual color discrimination. Trichromatic vision in humans, mediated by red-, green-, and blue-sensitive cones, enables high-acuity color discrimination, in contrast to the dichromatic vision observed in most other mammals. Beyond cone type, visual signaling is shaped by the spatial arrangement and connectivity of individual cones (Imamoto & Shichida, 2014). In heterozygous females harboring *ARR3* variants, random X-inactivation generates a retinal mosaic of cones expressing either the wild-type allele (produces normal amount of cone arrestin) or the mutant allele (loss of cone arrestin) (van Mazijk et al., 2022; Wang et al., 2023b). This heterogeneous activation pattern may create conflicting signals in visual phototransduction, leading to conflicting signals among neighboring cones and their downstream targets, such as bipolar and amacrine cells, potentially simulating optical defocus, promoting axial elongation, and enhancing myopic progression (Wang et al., 2023b).

PDE6H encodes the inhibitory subunit of cone-specific cGMP phosphodiesterase, a tetramer composed of two catalytic units (PDE6C) and two inhibitory units (PDE6H) (Gillespie & Beavo, 1988; Shimizu-Matsumoto et al., 1996). During phototransduction, light activation initiates the hydrolysis of cGMP to GMP by this enzyme complex, thereby mediating the conversion of light stimuli into neural signals (Biel & Michalakis, 2009). In darkness, photoreceptor cells with elevated cGMP levels maintain the opening of cyclic nucleotide-gated (CNG) channels, keeping photoreceptors in a depolarized state (Lamb, 2020; Leskov et al., 2000). Upon light exposure, PDE6H activity reduces intracellular cGMP concentrations, triggering CNG channel closure and cellular hyperpolarization, transmitting light signals to neural signals (Lamb, 2020). In the current study, scRNA-seq revealed down-regulation of both *Pde6h* and *Pde6c* in M/S cones of *Arr3*$^{+/-}$ rats compared to those of *Arr3*$^{+/+}$ and *Arr3*$^{-/0}$ rats. Notably, *Pde6c* expression was up-regulated in M/S cones of *Arr3*$^{-/0}$ rats, suggesting a potential compensatory response that may preserve phototransduction capacity in the absence of *Arr3* (Figure 6). This differential expression pattern implies that cone signaling balance may be more severely disrupted in heterozygous than in hemizygous mutants. These findings offer a molecular framework for understanding the mechanism of XLFL inheritance in *ARR3*-associated eoHM. Future investigations should characterize alterations in phototransduction dynamics and sensitivity, such as through patch-clamp electrophysiology or Ca^{2+} imaging in retinal slices from nonhuman primates or patient-derived human-induced pluripotent stem cell retinal organoids from *ARR3*-associated patients with eoHM (Ingram et al., 2019, 2020).

Although the findings of this study provide mechanistic insights into *ARR3*-associated XLFL inheritance, they are insufficient to directly explain the pathogenesis of eoHM in humans, as the rodent models did not exhibit an overt eoHM phenotype. This limitation is consistent with prior studies reporting absent or attenuated myopic features in rodent models carrying mutations in genes such as *RPGR* and *RP2*, both of which are causally linked to syndromic eoHM in humans (Lyraki et al., 2016). These observations highlight fundamental limitations of rodent systems in modeling monogenic eoHM, likely due to interspecies differences in retinal cell composition, macular structure, photoreceptive molecules, and anatomical disparities such as smaller eye size, relatively large lens volume, and reduced vitreous chamber depth (Troilo et al., 2019). In this study, rodents were selected due to the availability of *ARR3* mutation knock-in and knockout lines, their established utility in environment-induced myopia, and their accessibility for genetic manipulation. Despite the absence of a human-like macula, rodent retinas remain widely used for studying retinal signal processing and inheritance patterns. Myopia, including high myopia, is frequently observed in retinal disorders such as congenital stationary night blindness (CSNB) (Zeitz et al., 2023), and has been documented within the phenotypic spectra of retinal gene mutations, including *RPGR* (Di Iorio et al., 2020) and *GUCY2D* (Yi et al., 2021). Although the retina plays a central role in regulating ocular axial growth (Wallman & Winawer, 2004), the molecular pathways linking phototransduction to scleral remodeling remain poorly defined. *ARR3*-associated eoHM provides a rare genetic model for exploring early disruptions in cone-mediated visual signaling that may perturb emmetropization. This study established two rodent models to examine the impact of *ARR3*-associated XLFL inheritance on cone subtype function and patterning. However, the absence of L cones in rodents limits their utility for modeling red cone circuitry. Future work should incorporate induced myopia

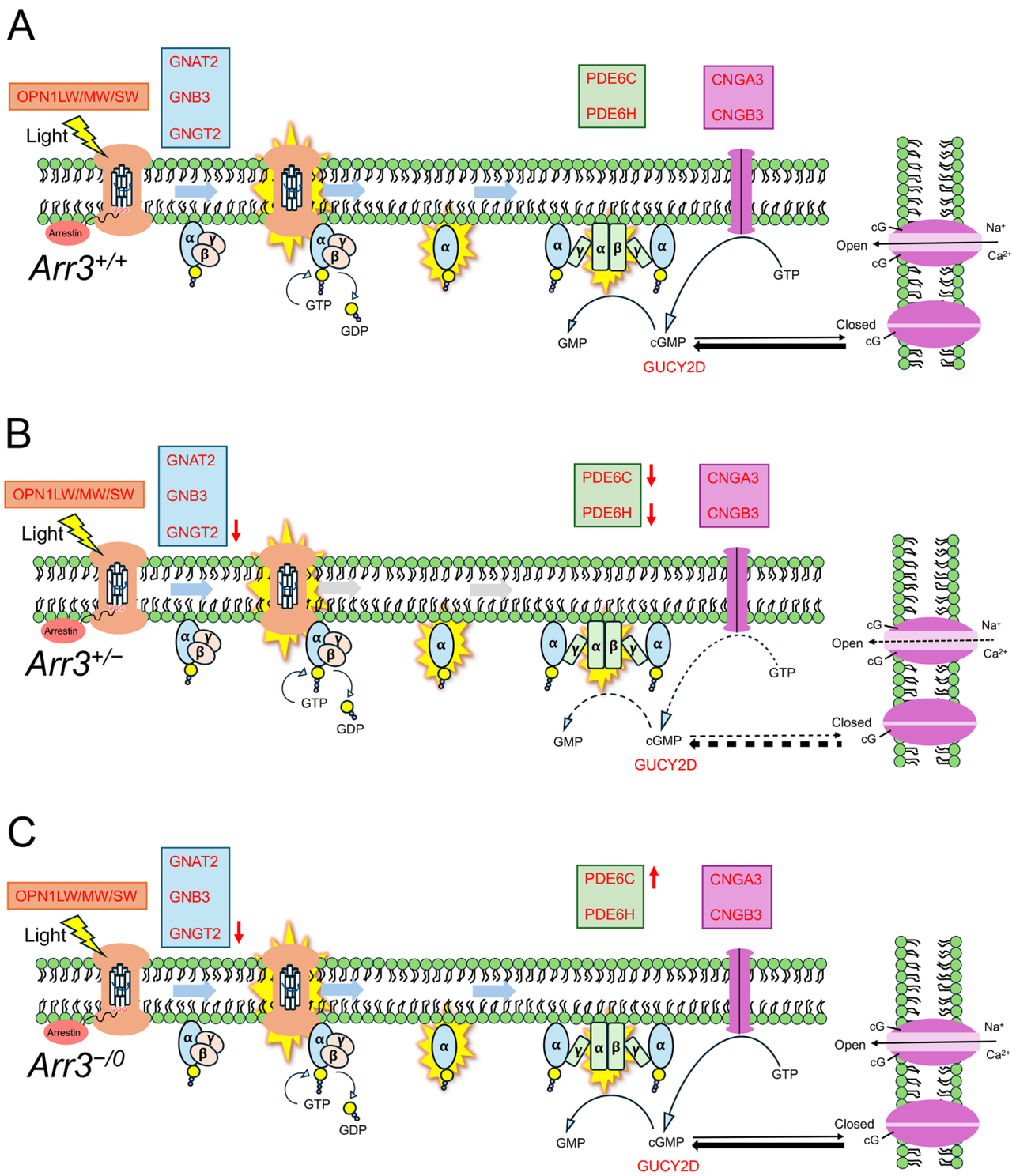

Figure 6 Schematic of phototransduction in M/S cones in rats of different *Arr3* genotypes

A: Schematic representation of phototransduction in wild-type rats (referenced from https://en.wikipedia.org/wiki/Visual_phototransduction). B: In *Arr3* heterozygous rats, mosaic expression of *Arr3* was accompanied by down-regulation of *Gngt2*, *Pde6c*, and *Pde6h*, potentially altering intracellular cGMP levels and the function of heterotetrameric CNG channels, thereby disrupting intracellular signaling and synaptic transmission to bipolar cells. C: In *Arr3* hemizygous rats, although *Gngt2* expression was down-regulated, up-regulation of *Pde6c* may compensate, partially maintaining signal transduction.

paradigms—such as lens defocus or spectral light manipulation—and apply more physiologically relevant systems, including nonhuman primates or patient-derived retinal organoids. These models would allow assessment of proportional and spatial changes in cone subtypes, particularly dorsal-ventral and central-peripheral gradients (Applebury et al., 2000; Daniele et al., 2011; Haverkamp et al., 2005; Lyubarsky et al., 1999; Nikonov et al., 2006). Critically, the downstream signaling mechanisms by which cone mosaicism—likely involving red cones—drives axial elongation (especially changes in choroid and sclera) remain undefined. Integrative analyses of cone–bipolar/amacrine cell networks in

primate or iPSC-derived retinal models may help delineate the functional and metabolic pathways linking cone phototransduction to posterior eye growth, ultimately identifying candidate targets for myopia intervention.

In summary, this study identified three principal findings, including the spatiotemporal co-labeled of Arr3 with red/green opsin in cones, the presence of mosaic Arr3 expression in *Arr3*$^{M/+}$ mice and *Arr3*$^{+/-}$ rats, and a marked reduction of M/S cones in *Arr3*$^{+/-}$ rats, accompanied by altered *Pde6h* expression involved in phototransduction. These results offer mechanistic insight into the unusual XLFL inheritance pattern and provide a foundation for studying myopia development through disruptions in retinal signal processing, particularly within cone pathways and their downstream neuronal connections.

DATA AVAILABILITY

The raw scRNA-seq data were deposited in the National Center for Biotechnology Information (NCBI) database (GSE309092), China National Center for Bioinformation database of Genome Sequence Archive (GSA) (CRA030269), and Science Data Bank (https://doi.org/10.57760/sciencedb.27890).

SUPPLEMENTARY DATA

Supplementary data to this article can be found online.

CONFLICTS OF INTEREST

The authors declare that they have no competing interests.

AUTHORS' CONTRIBUTIONS

Q.Z. and W.S. designed the study. Z.Y. and X.L. performed *Arr3* expression analysis. J.O., Z.Y., X.L., W.D., S.C., and Y.D. performed the mouse experiments. J.O., Z.Y., X.L., W.D., and Y.W. performed the rat experiments. J.O., G.W., Y.J., X.X., Q.Z., and W.S. performed the retinal scRNA-seq analysis. J.O., W.S., J.F.H. and Q.Z. discussed the results and wrote the manuscript. All authors read and approved the final version of the manuscript.

ACKNOWLEDGEMENTS

The authors are grateful to the staff of the Laboratory Animal Center at the State Key Laboratory of Ophthalmology, Zhongshan Ophthalmic Center, for technical support.

REFERENCES

Applebury ML, Antoch MP, Baxter LC, et al. 2000. The murine cone photoreceptor: a single cone type expresses both S and M opsins with retinal spatial patterning. *Neuron*, **27**(3): 513–523.

Biel M, Michalakis S. 2009. Cyclic nucleotide-gated channels. *In*: Schmidt HHHW, Hofmann F, Stasch JP. cGMP: Generators, Effectors and Therapeutic Implications. Berlin, Heidelberg: Springer, 111–136.

Brown PK, Wald G. 1964. Visual pigments in single rods and cones of the human retina. Direct measurements reveal mechanisms of human night and color vision. *Science*, **144**(3614): 45–52.

Carter-Dawson LD, Lavail MM. 1979. Rods and cones in the mouse retina. I. Structural analysis using light and electron microscopy. *The Journal of Comparative Neurology*, **188**(2): 245–262.

Cho A, Haruyama N, Kulkarni AB. 2009. Generation of transgenic mice. *Current Protocols in Cell Biology*, **Chapter 19**: Unit 19.11.

Daniele LL, Insinna C, Chance R, et al. 2011. A mouse M-opsin monochromat: retinal cone photoreceptors have increased M-opsin expression when S-opsin is knocked out. *Vision Research*, **51**(4): 447–458.

Deming JD, Pak JS, Brown BM, et al. 2015. Visual cone arrestin 4 contributes to visual function and cone health. *Investigative Ophthalmology & Visual Science*, **56**(9): 5407–5416.

Di Iorio V, Karali M, Melillo P, et al. 2020. Spectrum of disease severity in patients with X-linked retinitis pigmentosa due to *RPGR* mutations. *Investigative Ophthalmology & Visual Science*, **61**(14): 36.

Dibbens LM, Tarpey PS, Hynes K, et al. 2008. X-linked protocadherin 19 mutations cause female-limited epilepsy and cognitive impairment. *Nature Genetics*, **40**(6): 776–781.

Giansante G, Mazzoleni S, Zippo AG, et al. 2024. Neuronal network activity and connectivity are impaired in a conditional knockout mouse model with PCDH19 mosaic expression. *Molecular Psychiatry*, **29**(6): 1710–1725.

Gillespie PG, Beavo JA. 1988. Characterization of a bovine cone photoreceptor phosphodiesterase purified by cyclic GMP-sepharose chromatography. *The Journal of Biological Chemistry*, **263**(17): 8133–8141.

Gurevich EV, Gurevich VV. 2006. Arrestins: ubiquitous regulators of cellular signaling pathways. *Genome Biology*, **7**(9): 236.

Haarman AEG, Thiadens AAHJ, van Tienhoven M, et al. 2022. Whole exome sequencing of known eye genes reveals genetic causes for high myopia. *Human Molecular Genetics*, **31**(19): 3290–3298.

Hagen LA, Arnegard S, Kuchenbecker JA, et al. 2019. The association between L: M cone ratio, cone opsin genes and myopia susceptibility. *Vision Research*, **162**: 20–28.

Haverkamp S, Wässle H, Duebel J, et al. 2005. The primordial, blue-cone color system of the mouse retina. *The Journal of Neuroscience*, **25**(22): 5438–5445.

Hoshina N, Johnson-Venkatesh EM, Hoshina M, et al. 2021. Female-specific synaptic dysfunction and cognitive impairment in a mouse model of *PCDH19* disorder. *Science*, **372**(6539): eaaz3893.

Imamoto Y, Shichida Y. 2014. Cone visual pigments. *Biochimica et Biophysica Acta (BBA) - Bioenergetics*, **1837**(5): 664–673.

Ingram NT, Sampath AP, Fain GL. 2019. Voltage-clamp recordings of light responses from wild-type and mutant mouse cone photoreceptors. *The Journal of General Physiology*, **151**(11): 1287–1299.

Ingram NT, Sampath AP, Fain GL. 2020. Membrane conductances of mouse cone photoreceptors. *The Journal of General Physiology*, **152**(3): e201912520.

Lamb TD. 2020. Evolution of the genes mediating phototransduction in rod and cone photoreceptors. *Progress in Retinal and Eye Research*, **76**: 100823.

Leskov IB, Klenchin VA, Handy JW, et al. 2000. The gain of rod phototransduction: reconciliation of biochemical and electrophysiological measurements. *Neuron*, **27**(3): 525–537.

Li JL, Gao B, Guan LP, et al. 2015. Unique variants in *OPN1LW* cause both syndromic and nonsyndromic X-Linked high myopia mapped to MYP1. *Investigative Ophthalmology & Visual Science*, **56**(6): 4150–4155.

Li XX, Wang SY, Wang YH, et al. 2025. Clinical and molecular landscape of *GLRA2* in X-linked early-onset high myopia. *Investigative Ophthalmology & Visual Science*, **66**(4): 30.

Liu F, Wang JW, Xing YQ, et al. 2020. Mutation screening of 17 candidate genes in a cohort of 67 probands with early-onset high myopia. *Ophthalmic and Physiological Optics*, **40**(3): 271–280.

Lyraki R, Megaw R, Hurd T. 2016. Disease mechanisms of X-linked retinitis pigmentosa due to *RP2* and *RPGR* mutations. *Biochemical Society Transactions*, **44**(5): 1235–1244.

Lyubarsky AL, Falsini B, Pennesi ME, et al. 1999. UV- and midwave-sensitive cone-driven retinal responses of the mouse: a possible phenotype for coexpression of cone photopigments. *The Journal of Neuroscience*, **19**(1): 442–455.

Macosko EZ, Basu A, Satija R, et al. 2015. Highly parallel genome-wide expression profiling of individual cells using nanoliter droplets. *Cell*, **161**(5): 1202–1214.

McClements M, Davies WI, Michaelides M, et al. 2013. Variations in opsin

coding sequences cause x-linked cone dysfunction syndrome with myopia and dichromacy. *Investigative Ophthalmology & Visual Science*, **54**(2): 1361–1369.

Murakami A, Yajima T, Sakuma H, et al. 1993. X-Arrestin: a new retinal arrestin mapping to the X chromosome. *FEBS Letters*, **334**(2): 203–209.

Nikonov SS, Brown BM, Davis JA, et al. 2008. Mouse cones require an arrestin for normal inactivation of phototransduction. *Neuron*, **59**(3): 462–474.

Nikonov SS, Kholodenko R, Lem J, et al. 2006. Physiological features of the S- and M-cone photoreceptors of wild-type mice from single-cell recordings. *The Journal of General Physiology*, **127**(4): 359–374.

Shimizu-Matsumoto A, Itoh K, Inazawa J, et al. 1996. Isolation and chromosomal localization of the human cone cGMP phosphodiesterase γ cDNA (PDE6H). *Genomics*, **32**(1): 121–124.

Széll N, Fehér T, Maróti Z, et al. 2021. Myopia-26, the female-limited form of early-onset high myopia, occurring in a European family. *Orphanet Journal of Rare Diseases*, **16**(1): 45.

Taylor CP, Shepard TG, Rucker FJ, et al. 2018. Sensitivity to S-cone stimuli and the development of myopia. *Investigative Ophthalmology & Visual Science*, **59**(11): 4622–4630.

Troilo D, Smith III EL, Nickla DL, et al. 2019. IMI - report on experimental models of emmetropization and myopia. *Investigative Ophthalmology & Visual Science*, **60**(3): M31–M88.

van Mazijk R, Haarman AEG, Hoefsloot LH, et al. 2022. Early onset X-linked female limited high myopia in three multigenerational families caused by novel mutations in the *ARR3* gene. *Human Mutation*, **43**(3): 380–388.

Wallman J, Winawer J. 2004. Homeostasis of eye growth and the question of myopia. *Neuron*, **43**(4): 447–468.

Wang PF, Xiao XS, Huang L, et al. 2013. Cone-rod dysfunction is a sign of early-onset high myopia. *Optometry and Vision Science*, **90**(11): 1327–1330.

Wang YW, Sun WM, Xiao XS, et al. 2023a. Unique haplotypes in *OPN1LW* as a common cause of high myopia with or without protanopia: a potential window into myopic mechanism. *Investigative Ophthalmology & Visual Science*, **64**(4): 29.

Wang YW, Xiao XS, Li XQ, et al. 2023b. Genetic and clinical landscape of *ARR3*-associated MYP26: the most common cause of Mendelian early-onset high myopia with a unique inheritance. *British Journal of Ophthalmology*, **107**(10): 1545–1553.

Xiao XS, Li SQ, Jia XY, et al. 2016. X-linked heterozygous mutations in *ARR3* cause female-limited early onset high myopia. *Molecular Vision*, **22**: 1257–1266.

Yi Z, Ouyang JM, Sun WM, et al. 2020. Comparative exome sequencing reveals novel candidate genes for retinitis pigmentosa. *eBioMedicine*, **56**: 102792.

Yi Z, Sun WM, Xiao XS, et al. 2021. Novel variants in *GUCY2D* causing retinopathy and the genotype-phenotype correlation. *Experimental Eye Research*, **208**: 108637.

Yuan DJ, Yan TZ, Luo SQ, et al. 2021. Identification and functional characterization of a novel nonsense variant in *ARR3* in a southern Chinese family with high myopia. *Frontiers in Genetics*, **12**: 765503.

Zeitz C, Roger JE, Audo I, et al. 2023. Shedding light on myopia by studying complete congenital stationary night blindness. *Progress in Retinal and Eye Research*, **93**: 101155.

Zhang HB, Cuenca N, Ivanova T, et al. 2003. Identification and light-dependent translocation of a cone-specific antigen, cone arrestin, recognized by monoclonal antibody 7G6. *Investigative Ophthalmology & Visual Science*, **44**(7): 2858–2867.